Smart Materials and
Structures

Paediatric ankle rehabilitation system based on twisted and coiled polymer actuators

To cite this article: Alberto Gonzalez-Vazquez *et al* 2024 *Smart Mater. Struct.* **33** 075009

OPEN ACCESS
IOP Publishing

Smart Materials and Structures

Smart Mater. Struct. **33** (2024) 075009 (14pp)

https://doi.org/10.1088/1361-665X/ad50b0

Paediatric ankle rehabilitation system based on twisted and coiled polymer actuators

Alberto Gonzalez-Vazquez, Lorenzo Garcia*[*] and Jeff Kilby

School of Engineering, Computer and Mathematical Sciences, Auckland University of Technology, Auckland, New Zealand

E-mail: lorenzo.garcia@aut.ac.nz

Received 15 December 2023, revised 16 May 2024
Accepted for publication 27 May 2024
Published 6 June 2024

Abstract

Rehabilitation is crucial for children with physical disabilities arising from various conditions. Traditional exoskeletons, reliant on electric motors and rigid components, making them cumbersome, heavy, and unsuitable for use outside clinical facilities. To overcome these, researchers are turning to soft wearable rehabilitation robots (SWRRs) with artificial muscles based on smart materials like twisted and coiled polymer actuators (TCPs). TCPs offer enhanced compliance, adaptability, comfort, safety, and reduced weight—critical for paediatric use. Despite facing challenges like low operating frequencies and high temperatures, TCPs are explored as potential artificial muscles for SWRRs, due to their advantages on the force they can generate, the strain and a linear behaviour. This study details a proof of concept for a paediatric rehabilitation system for ankles based on TCPs, including the actuator characterization, mechanical design, control strategy, and human-computer-interface (HCI). The resulting device achieved a 1.4 Nm torque, a 10° range of motion in dorsiflexion within 5 s, and integrated electromyographic HCI. This research marks a promising step towards innovative, soft wearable rehabilitation solutions for children with physical disabilities.

Supplementary material for this article is available online

Keywords: artificial muscles, exoskeletons, soft robotic, twisted and coiled polymer actuator, rehabilitation

1. Introduction

Ongoing paediatric physical disabilities can result from various causes, including neurological conditions like Cerebral Palsy [1], strokes [2], acquired brain injuries [3], neuromuscular diseases such as Duchenne muscular dystrophy [4] and spinal muscular atrophy [5], as well as traumatic injuries. Children with physical disabilities often face limitations in performing daily activities independently, which can impede their typical development. Mobility and exploration are crucial aspects of a child's development, contributing to cognitive, physical, social, and emotional growth [6].

Rehabilitation plays a vital role in assisting these children in recovering or maintaining functionality, enabling them to interact with their environment, and ultimately improving their quality of life and autonomy [7]. Rehabilitation exoskeletons have gained significant attention for their potential to address mobility challenges in individuals with physical disabilities. They offer advantages such as enabling extensive

---

[*] Author to whom any correspondence should be addressed.

practice for children with substantial disabilities, reducing the effort required from therapists during exercises, and providing a quantitative assessment of the patient's motor function [8].

However, most existing rehabilitation exoskeletons rely on electric motors and rigid components for their functionality. Unfortunately, these designs are often cumbersome, heavy, and unsuitable for use outside clinical facilities [9]. To overcome these limitations, researchers are now focusing on developing soft wearable rehabilitation robots (SWRRs) that incorporate artificial muscles based on smart materials (AMSMs). AMSM provides increased compliance, adaptability, comfort, safety, and reduced weight [10].

Due to this advantages they are interesting to be used in paediatric devices as the main characteristics that differentiate them from the adults version are safety, operability, weight and motivation [11]. Safety can be improved thanks to the compliance of the materials [12]. And the weight can be reduce drastically preventing abnormal movements pattern and increase energy consumption [13, 14]. Due to this advantages they are interesting to be used in paediatric devices as the main characteristics that differentiate them from the adults version are safety, operability, weight and motivation [11]. Safety can be improved thanks to the compliance of the materials [12]. And the weight can be reduce drastically preventing abnormal movements pattern and increase energy consumption [13, 14].

AMSMs are soft actuators composed primarily of material with a low Young's modulus like that of soft biological materials (10^4–10^9 Pa) that can sense and directly convert physical stimulus (e.g. light, electrical, heat) into physical displacement [15–17].

Shape memory alloys (SMAs) [18] and dielectric elastomer actuators (DEAs) [19] are indeed promising AMSM solutions for SWRR. However, they each have limitations that hinder their widespread use in this context.

DEAS present desirable characteristics with strain reaching 200%, a high bandwidth up to the range of kHz and high efficiency [20–22]. However, DEAs need high voltage, in the order of hundreds of volts, requires bulky and expensive electronics. Moreover, DEAs are challenging to produce in a compact size to generate appropriate amounts of power and force [23, 24].

SMAs present the advantages of power density and stress, these being as high as 50 W g^{-1} and 200 MPa, respectively [22, 25]. These advantages have made them the most popular option on SWRR prototypes [10]. However, they have limitations to be used on SWRR, as they have low efficiency, a small strain range (up to 8%) and high thermal hysteresis making them difficult to control [20, 22, 23]. SMAs present the advantages of power density and stress, these being as high as 50 W g^{-1} and 200 MPa, respectively [22, 25]. These advantages have made them the most popular option on SWRR prototypes [10]. However, they have limitations to be used on SWRR, as they have low efficiency, a small strain range (up to 8%) and high thermal hysteresis making them difficult to control [20, 22, 23].

Another noteworthy type of AMSM is the twisted and coiled polymer actuator (TCP). TCPs are created by twisting precursor polymer fibres and applying heat treatment [26]. To activate TCPs, an external heat source, such as metallic wires, is employed to induce joule heating, thereby enabling precise electrical control. TCPs offer several advantages, including high power density (27 W g^{-1}), stress (10 MPa), strain capacity (21%), and linear behaviour with minimal hysteresis. However, they do face certain limitations, such as low operating frequencies ($<$1 Hz), low power efficiency ($<$1.32%) and high operating temperatures ($>$80 °C) [20, 22, 27]. Due to their advantages three promising examples of wearable devices based on TCPs were founded:

Sutton *et al* [28] developed an assistive wrist orthosis with a single degree of freedom. This device employed 16 TCP) actuators made of silver-coated Nylon 6.6 sewing thread. It generated a torque of 0.3 Nm to the wrist joint in the flexion direction within 3.9 s. They implemented a proportional–integral–derivative (PID) controller to accurately follow a 0.1 Hz sinusoidal signal with a 10 N amplitude. The prototype was able to track the movement during activation but encountered challenges with slow response times during the relaxation phase.

IGrab [27], an ergonomic orthotic device to assist in finger flexion and extension movements, was designed by Saharan *et al.* The device featured a combination of 3D-printed components and sewn parts, including artificial tendons routed from the fingers to the wrist. The finger tendons were linked to TCP actuators, which were mounted on a forearm bracelet. Frictionless pulleys optimised TCP actuation, and rubber strips enhanced energy efficiency. When applying a 0.6 A step signal, the fingers reached their maximum displacements within 25 s (i.e. the index finger was able to move 40° for the metacarpophalangeal joint, 21° for the proximal interphalangeal joint, and 11° in the case of the distal interphalangeal joint), with further improvements observed when using pulsed signals, reducing actuation time to under 5 s.

Patiño *et al* [29] developed a wearable orthotic device for hand rehabilitation featuring individual TCP actuators for each finger. The orthosis consisted of two main components: one fitted to the dorsum of the hand and another for the fingers. Each finger incorporated a silicone tube housing a TCP and a filament strain sensor. The TCP actuators within the finger structure could generate forces of approximately 3 N when a 0.3 A step input was applied.

The orthotic devices mentioned demonstrate the application of TCPs in hand and wrist rehabilitation. However, there is a notable absence of studies exploring the feasibility of TCP utilization in the lower limb or paediatric systems. Moreover, previous literature has extensively investigated TCP as an actuation type and its mechanical design (inherent to the explored joint). Nevertheless, other critical components remain insufficiently explored in these works. These unexplored parameters may include considerations related to control strategy and human-computer interface (HCI), which are crucial for successfully developing and implementing paediatric SWRR systems [11, 30] (figure 1).

This paper explores the feasibility of TCPs as artificial muscles to drive SWRRs for children with physical disabilities. It highlights the advantages and the current limitations of TCPs on SWRR. The paper presents the design process of

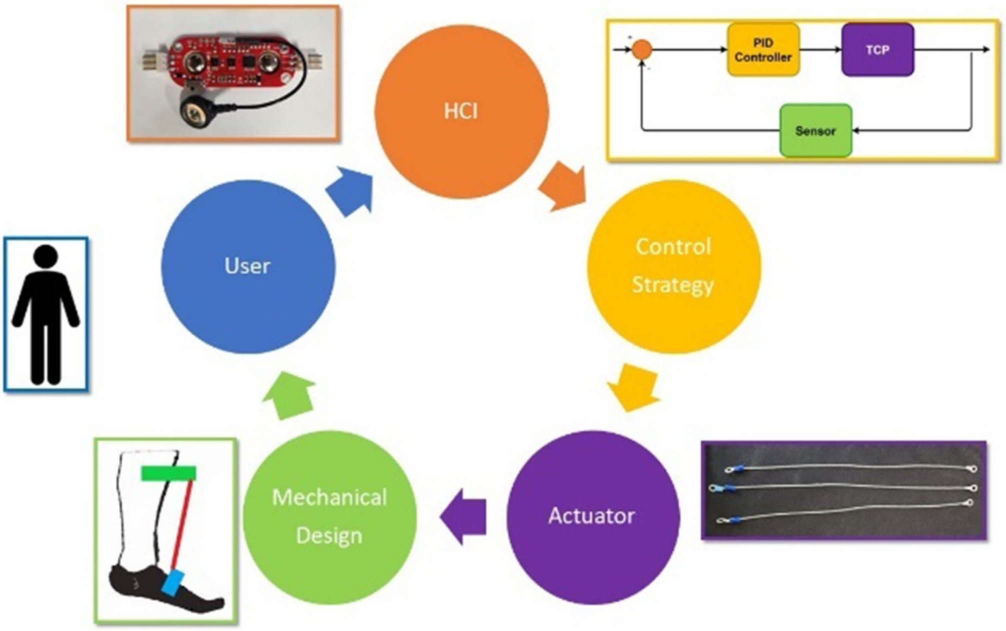

Figure 1. SWRR components.

a prototype for paediatric ankle SWRRs based on TCPs covering the main parameters of SWRRs being the actuator characterization, the mechanical design based on the biomechanical requirements for paediatric ankle dorsiflexion, the implementation of a control strategy that is merged with an HCI, with this covering the essential parameters that require a paediatric SWRR.

2. Design of the device and methods

This section presents a description of the TCP manufacturing process and its behaviour. Then, the biomechanical structure of the ankle and a dummy based on it are given as they are required to design and test the SWRR. Later, the design process of the SWRR is presented. Finally, the behaviour of the prototype and a mathematical model are shown.

2.1. TCPs manufacturing

The TCP actuators were fabricated using the process similar to Chossat *et al* [31]. A 1.5 m Nylon fishing line as the precursor fibre (EDGE Mono trace 80 LB) with a diameter of 840 μm. The nylon fibres were twisted and coiled alongside a 36 AWG (127 μm) Nickel–Chromium 80 (NiCr) wire (Fogslord). One end of the nylon fibre was firmly attached to the output shaft of a NEMA17 motor, while the other end was connected to a slider carrying a 1000 g weight (17.68 MPa, value according with: Force (1 Kg*9.8 m s^{-2})/ Fibre Cross Sectional Area ($\pi^{*}(420 \times 10^{-4}\ \mathrm{m})^{2}$)). The NiCr wire was also suspended from the motor shaft but was only weighted with 1.6 g (1.2 MPa) to maintain it in a straightened state. The nylon fibres were twisted and coiled at a slow rotation speed of 250 RPM. The twisting and coiling process was stopped manually once the precursor fibre was fully coiled.

Table 1. TCP manufacturing parameters.

Parameter	Value
Precursor fibre material	Nylon
Precursor fibre diameter (mm)	0.84
Precursor fibre length (mm)	1500
Precursor fibre tension (g MPa^{-1})	1000/17.68
Resistance wire material	Nichrome 80
Resistance wire diameter (AWG $\mu\mathrm{m}^{-1}$)	36/127
Resistance wire length (mm)	1670
Resistance wire tension (g MPa^{-1})	1.6/1.2
RPM	250
Motor turns	726 ± 6
TCP after coiling length (mm)	375 ± 5
TCP after annealing length (mm)	440 ± 5
Annealing current (mA)	240
TCP resistance (Ω)	137.1 ± 7.8
TCP DIAMETER (MM)	1.97 ± 0.04

For the annealing process, the embedded NiCr wire was employed to produce Joule heating. This annealing process consisted of five consecutive five-minute periods, each applying an annealing current of 240 mA. A 1 min cooling phase was inserted between each annealing period. After this treatment, TCPs with an average length of 44 cm and a diameter of 1.97 ± 0.04 mm were produced, the measurement were taken with a digital calliper (Duratool). The resulting actuators were trimmed to 39.5 cm and clamped with insulated male spade electric terminals. Each electrical terminal required 5 mm for crimping, which led to a 10 mm reduction in the functional area. Table 1 depict the main manufacturing parameters of the fabricated TCPs.

To test the fabricated samples, a custom-made experimental test bench was utilised to measure force and displacement

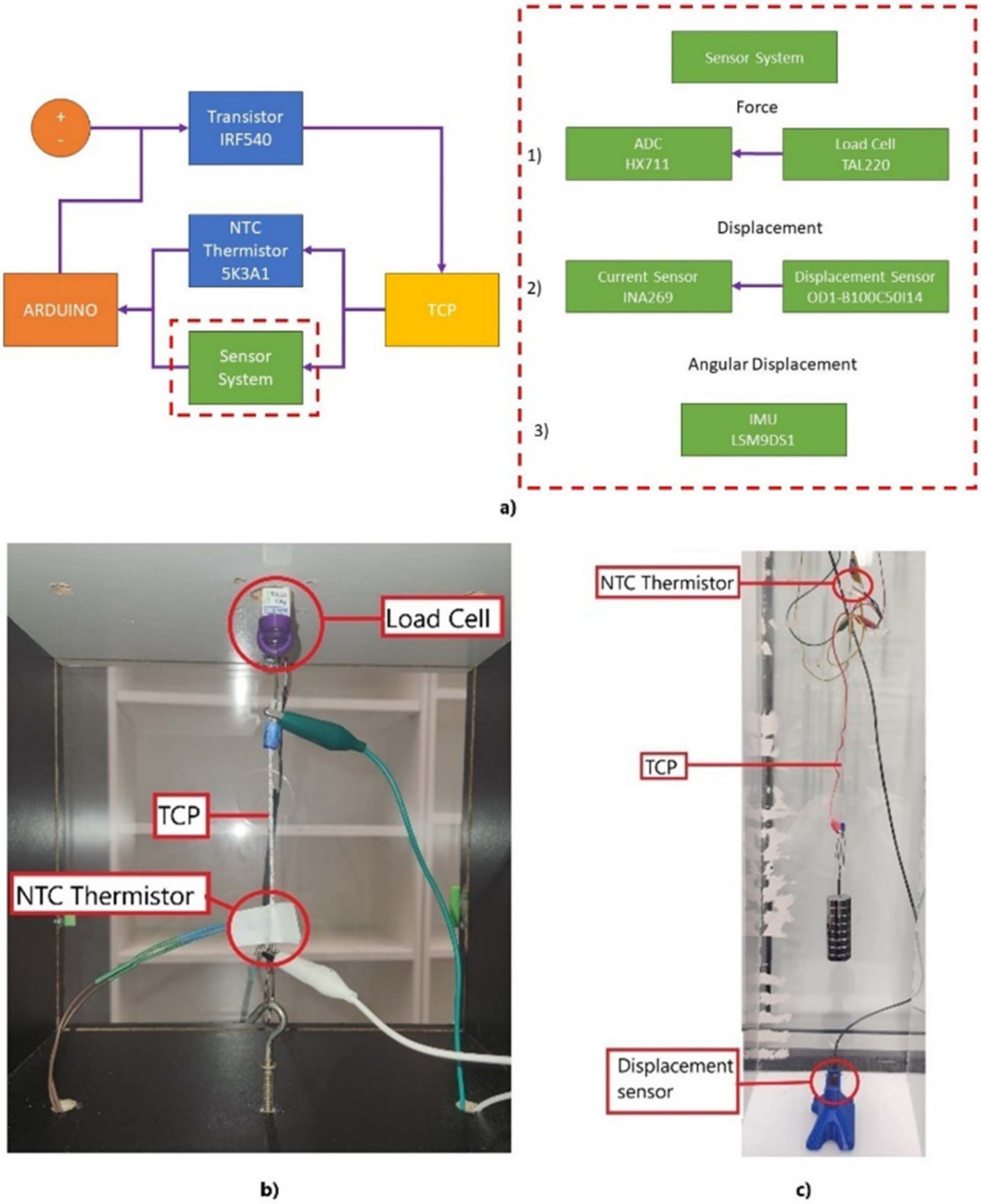

Figure 2. (a) Test bench block diagram for (1) force, (2) displacement and (3) angular displacement test. (b) Force test bench. (c) Displacement test bench.

(figure 2(a)). In both cases, an Arduino NANO served as the data acquisition system. A transistor (Vishay Siliconix IRF540) regulated the voltage from the power supply, while an NTC thermistor (TE Connectivity, 5K3A1) was employed to monitor the temperature of the TCP.

In the force test (figure 2(b)), one end of the actuator was fastened to a fixed hook, and the other end was connected to a 10 Kg load cell (TAL220). This load cell was interfaced with the Arduino through an analogue-to-digital converter (Avia semiconductor, HX711). For the displacement test (figure 2(c)), the actuator was suspended with a weight above a laser displacement sensor (Sick OD mini OD1-B100C50I14), which was connected to a current sensor (Texas Instruments INA269) interfacing with the Arduino. The calibration process for the sensor can be found in the supplementary information (Calibration Procedures).

Both force and displacement tests applied a square signal of 2400 s on and 240 s off to observe the strain and power relationship. The 240 s duration was chosen to allow the system to reach a stable condition. Experiments were repeated at different power levels ranging from 160 mA to 240 mA with the applied current incrementing by 20 mA.

Throughout the experiments, data on TCA temperatures, power consumption, and the weight distance from the sensor were continuously recorded using an Arduino NANO with a sampling time of 50 ms. In the case of the displacement test, various weight values ranging from 600 g to 1000 g were employed to assess the actuator's performance. Each test

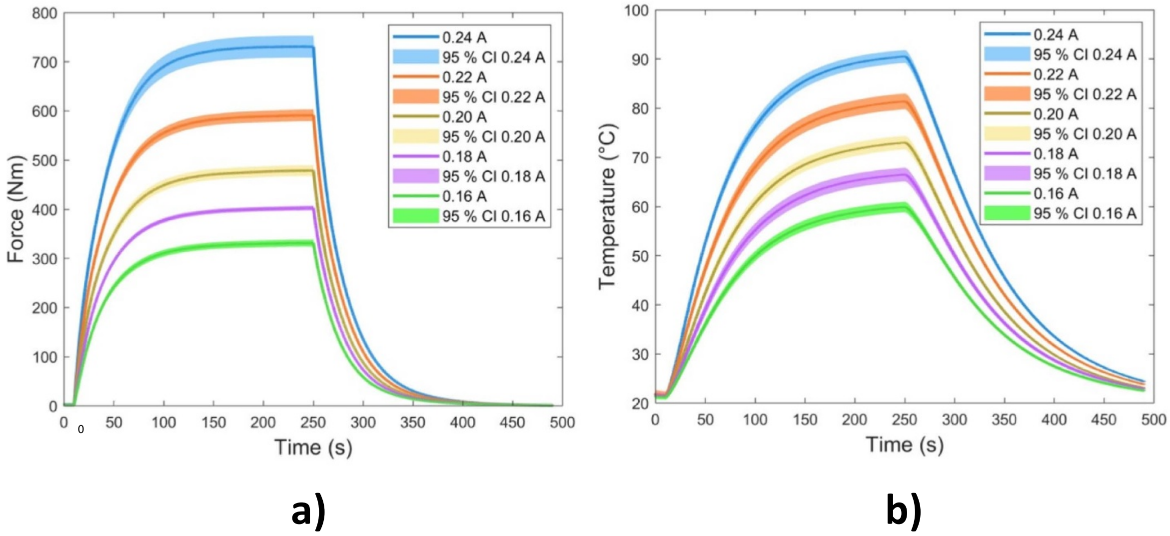

Figure 3. Force power relationship (a) and temperature power relationship during the isotonic force test. Confident intervals (CI) included.

(force and strain) was performed using 5 different actuators, each one used 4 times, for 20 trials per test.

2.2. TCP behaviour

Characterising the performance of the manufactured actuators is essential to determine their suitability for the SWRR requirements. In these tests using TCPs as linear actuators, two primary parameters of interest are force and strain, which will later be converted into torque and range of motion (ROM). The mean of the last 50 samples before turning off the applied power was averaged to calculate the maximum in both tests. This average represents the system's steady state after the step signal was applied. Then, from the 20 maximum values, the mean and standard deviation of the maximum force, temperature, displacement, and strain were obtained.

Figure 3 displays the results obtained from the force test. The TCP actuator's maximum force output is 7.9 ± 0.5 N (807.9 ± 57.6 g) when a current of 240 mA is applied. However, it is important to note that when considering the prestress of the fibre (0.7 ± 0.2 N or 76.8 ± 21.2 g), the maximum change in force is 7.1 ± 0.4 N (730.0 ± 46.3 g) (figure 3(a)). To assess the response times for heating (τ_h) and cooling (τ_c), the analysis focused on the average time required for the actuator to reach 63% of a steady-state value after a step input. The analysis results indicate that the average τ_h is 31.42 ± 1.02 s, and τ_c is 28.2 ± 0.4 s. At the highest applied power level, the generated temperature reached 78.35 °C ± 2.07 °C (figure 3(b)).

In contrast, the results from the displacement test highlight the noticeable impact of pre-strain (generated by the weights) on the actuator's length, causing it to contract from 386.0 ± 3.7 mm to 380.2 ± 3.7 mm, 373.88 ± 4.08 mm, 365.3 ± 4.8 mm, 357.9 ± 5.3 mm. This pre-strain has a direct effect on the actuator's contraction. When a current of 240 mA was applied with different loads, the maximum displacements were as follows 38.7 ± 1.9 mm, 39.8 ± 0.8 mm, 40.4 ± 2.1 mm, 43.5 ± 2.4 mm, 44.5 ± 1.1 mm for weights of 1000 g, 900 g, 800 g, 700 g, and 600 g, respectively (figure 4(a)). Nevertheless, when the final elongation is considered, the strain can be obtained using the following formula:

$$S = \frac{\Delta L}{L} X100. \qquad (1)$$

Here, strain (S) represents the relationship between the initial length (L) of the actuator and the resulting stroke (ΔL) when activated, expressed as a percentage. Analysing the strain data, the results were as follows: 10.02% ± 0.45%, 10.4% ± 0.1%, 10.9% ± 0.6%, 11.7% ± 0.7%, 12.3% ± 0.3% for weights of 1000 g, 900 g, 800 g, 700 g, and 600 g, respectively (figure 4(b)). It is noteworthy that these strain values align with the findings from the maximum force analysis, where the maximum generated force was observed at 7.1 N (730.0 ± 46.3 g). After this point is possible to see a fall in the displacement and strain. The average response times (τ_h) and (τ_c) are measured at 39.2 ± 1.3 s and 20.6 ± 0.5 s, respectively.

2.3. Ankle biomechanics

The ankle, characterised by its intricate anatomy, comprises the tibiotalar joint and the transverse tarsal joint, collectively affording a broad spectrum of multidirectional motion. Critical motions within the ankle joint complex encompass plantar- and dorsiflexion, occurring predominantly in the sagittal plane, as well as ab-/adduction in the transverse plane and inversion-eversion in the frontal plane. Combinations of rotations across the subtalar and tibiotalar joints generate three-dimensional motions called supination and pronation [32, 33].

However, it is worth mentioning that the majority of ankle movement primarily occurs within the sagittal plane, with plantar and dorsiflexion being predominantly governed by the

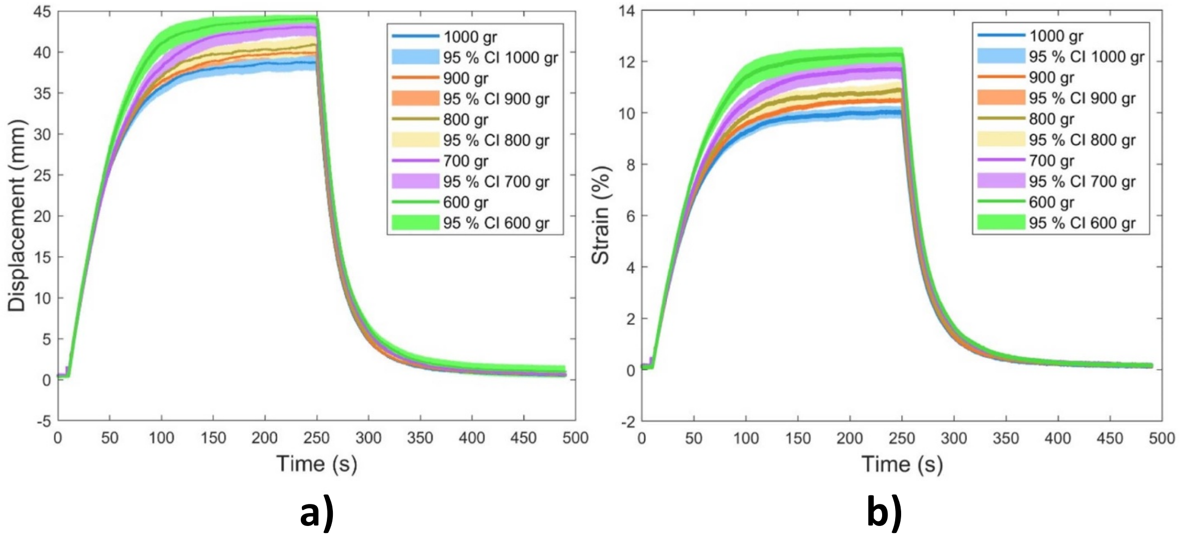

Figure 4. (a) Displacement-weight relationship and (b) strain-weight relationship. Confident intervals (CI) included.

tibiotalar joint. The total ankle ROM in the sagittal plane typically spans from 65° to 75°, encompassing 25° to 30° of dorsiflexion and 40° to 45° of plantarflexion. Nevertheless, during activities like walking, the required ROM in the sagittal plane is considerably reduced to approximately 25°. In this context, adult ankles generally move from 20° of plantar flexion to 10° of dorsiflexion, while children exhibit a range of 5° dorsiflexion. Regarding ankle stiffness, which pertains to the mechanical resistance to passive movement, achieving 10° of dorsiflexion necessitates 6.21 Nm of torque for adults, whereas children require 1.5 Nm [34, 35].

The plantar-dorsiflexion movement within a 66° range is commonly observed during daily activities such as walking, climbing stairs, etc. These activities typically occur at a frequency of around 1.75 Hz. However, it is important to note that during rehabilitation sessions, these movements are often executed at much lower frequencies, usually falling below 0.2 Hz [10, 36, 37].

2.4. Dummy testing platform

For conducting trials on the paediatric ankle SWRR, a mannequin designed to replicate the lower limb proportions of an average 10 year-old child was employed. Accurate measurements for the leg were derived from the World Health Organization's (WHO) child growth standards [38] and the anthropometric data provided by Winters [39]. These references guided the determination of limb dimensions, resulting in a crus length (knee to ankle) of 40 cm, foot length and width of 22 cm and 7 cm respectively. Thet total foot weight 300 g. The used dummy is shown in figure 5.

To assess the exoskeleton's response to various torques, diverse weights were added to the foot, situated 10 cm from the ankle's centre of rotation. The weights ranged from 500 g to 3000 g, incremented in 500 g intervals. This weight variation corresponded to a torque spectrum from 3 Nm to 0.5 Nm.

2.5. Paediatric ankle SWRR design

The SWRR consisted of two 3D-printed braces that wrapped around the top part of the crus brace (CB) and the second one on top of the foot instep brace (FIB), figure 5. The FIB was positioned 5 cm away from the centre of rotation of the ankle. Both braces use Velcro to maintain the position over the mannequin. Furthermore, the braces are divided into two different parts: the brace and the lid. This design allowed the connection of the TCPs in series using copper tape between both parts as the electrical connection. The computer-aided design (CAD) model of both braces is displayed in figure 5. The entire device weight was 300 g (without a power supply or battery), making each brace weight 150 g.

On figure 6 an ankle model is showed. P1 is the point at where the TCPs are connected to FIB, P2 is the point where the TCP is connected to CB and $P0$ the point at the centre of rotation with coordinate (0,0). The coordinate of $P1$ (X_{p1}, Y_{p1}) is:

$$X_{p1} = r\cos\theta_1,\, Y_{p1} = r\sin\theta_1 \tag{2}$$

Then L_{Tcp} can be written as:

$$L_{Tcp} = \sqrt{(L_H - X_{p1})^2 + (L_V + Y_{p1})^2}. \tag{3}$$

And θ_2:

$$\theta_2 = \tan^{-1}\left(\frac{L_V + Y_{p1}}{L_H - X_{p1}}\right) \tag{4}$$

where r is the radius between the centre of rotation and $P1$, θ_1 is the angle of the foot during dorsiflexion, θ_2 is the angle between the TCPS and the braces, L_V is the distance between $P1$ and $P2$ when $\theta_1 = 0$, L_H is the distance between the centre of rotation and the connection of the TCP on CB (x axis). Finally, L_{Tcp} is the length of the TCPs.

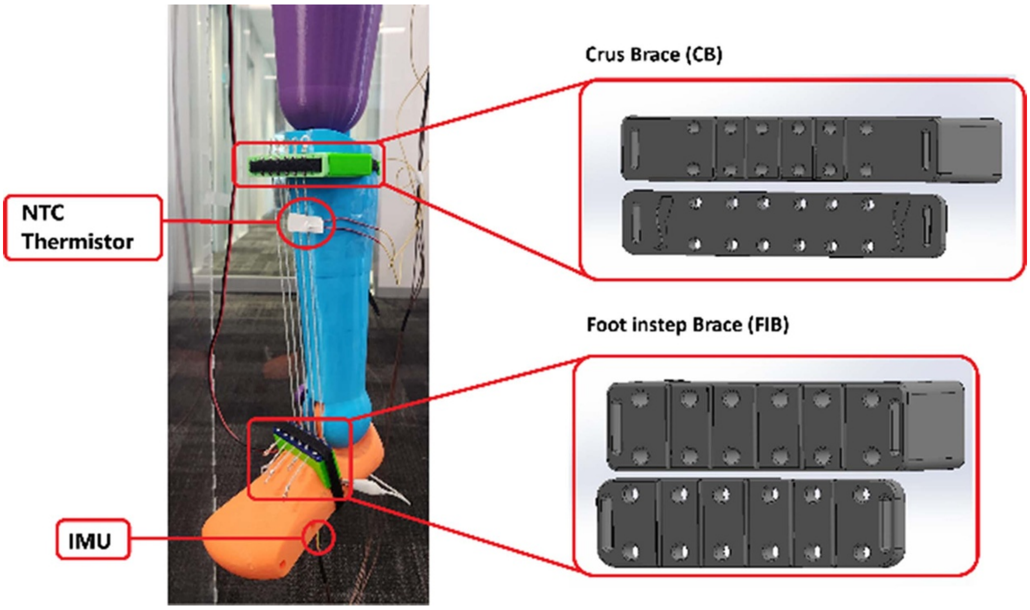

Figure 5. Paediatric leg dummy and CAD design of the SWRR braces.

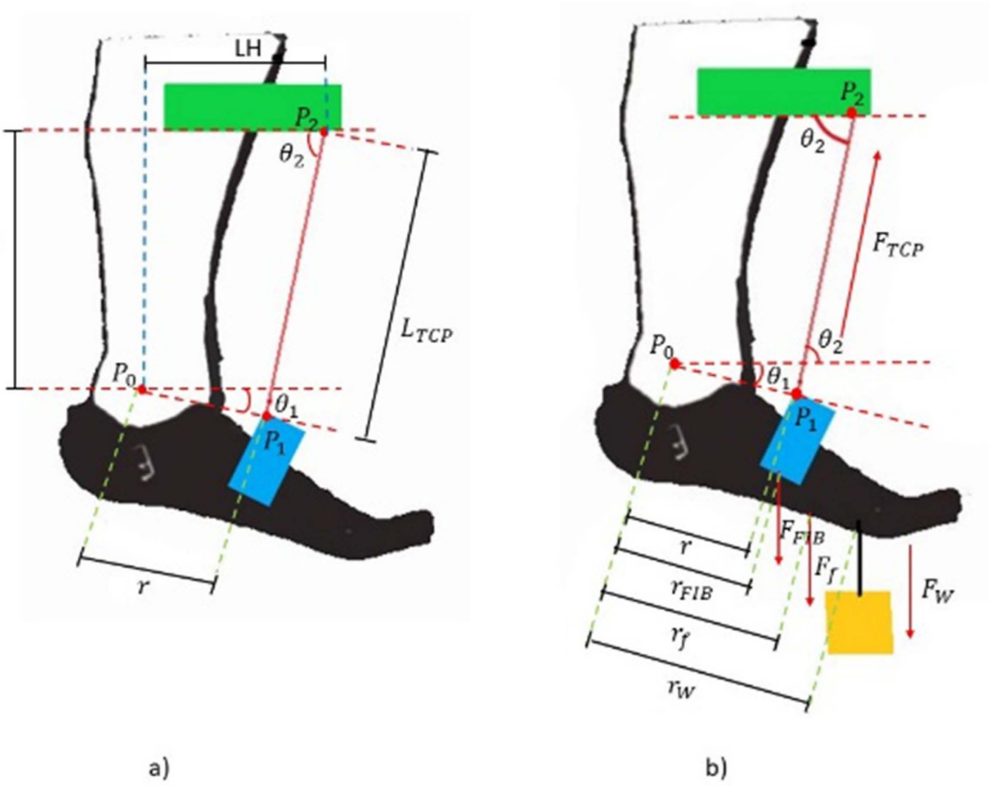

Figure 6. Free body diagram for (a) displacement and (b) forces acting on the dummy.

In the case of the generated Torque (T), the system can be evaluated as follows:

$$T = F_{\mathrm{TCP}}\, x \sin\theta_2 x r x \cos\theta_1 - F_w x r_w x \cos\theta_1 - F_f x r_f x \cos\theta_1 - F_{\mathrm{FIB}}\, x r_{\mathrm{FIB}}\, x \cos\theta_1 \quad (5)$$

where F_W is the force generated by the weight used on the experiments, r_W the distance of the weight to the centre of rotation, F_f is the force generated by the weight of the foot and r_f is the foot centre of gravity, F_{FIB} is the force generated by the weight of the FIB and r_{FIB} the distance of the weight to the centre of rotation, F_{TCP} is the force generated by the TCPs.

With the mechanical model of the SWRR, the behaviour of the TCP and the requirements given in section 2.3. Then The SWRR was designed to provide dorsiflexion movement of children with the following characteristics: (i) being able to provide an angular displacement of 10° in the plantarflexion direction, (ii) providing a torque of 1.5 Nm. Hence, five TCPs of 30 cm, when unloaded, were used for this. The number of fibres was constrained to five as the biggest challenge for TCPs is the speed. Keeping in mind that the width of the leg was 7 cm, a gap of 12 mm was left to prevent heat crosstalk and improve the cooling time [40]. Furthermore, this study is centred on reaching frequencies that can be used in a rehabilitation set-up of 0.2 Hz. Hence, a PID controller was developed to achieve the desired angular displacement in 5 s (section 3).

2.6. SWRR test

The performance assessment of the paediatric ankle SWRR was carried out using the testing setup described in section 2.4. The electronic components used were nearly identical to those employed in the force and displacement tests for the unit TCP. These components included an Arduino, a MOSFET, and a thermistor. However, a key distinction lies in the sensor utilised to record angular displacement (figure 2). To fulfil this purpose, a 9-degree-of-freedom Inertial Measurement Unit (IMU), was employed (LSM9DS1, STMicroelectronics).

Both testing procedures followed the application of a square signal, consisting of 180 s on and 180 s off, to establish the strain-power relationship. The selection of the 180 s duration allowed sufficient time for the system to reach a stable equilibrium. The experiments were conducted across various current levels, spanning from 160 mA to 240 mA (incrementally adjusted by increasing the current in 20 mA steps), encompassing all the different TCP actuators. Throughout the test, data about TCA (Thermally Activated Contractile) temperatures, power consumption, and the angular displacement of the foot were recorded and stored on a computer, with the data acquisition performed using an Arduino NANO at a sampling rate of 50 ms. The testing protocol encompassed a range of torque conditions, spanning from 0.5 Nm to 3.0 Nm in 0.5 Nm increments. In addition to the torque generated by the load, it is essential to account for the total negative torque produced by the combined weight of the foot and the FIB (300 g from the dummy and 150 g from FIB), which amounts to approximately 0.4 Nm. Each test was conducted four times utilizing the identical set of actuators. The mean of the last 50 samples before deactivating the applied power was computed to determine the maximum in both tests. This average reflects the system's steady state following the application of the step signal. Subsequently, from the 4 maximum values obtained, the mean and standard deviation of the maximum angular displacement, and temperature were calculated.

The results depicted in figure 7(a) sows the effect of the load on the TCPs fibres, stretching the fibres decreasing the initial starting point to −15, −27°, −33°, −37.5°, −40° and −42.5° respectively to the applied torque of 0.5 Nm, 1 Nm, 1.5 Nm, 2 Nm, 2.5 Nm, and 3 Nm. After removing this offset figure 7(b) illustrate that the maximum ROM was attained under a 1.0 Nm load. These findings align with the design objectives, as they are closest to the specified 1.5 Nm torque requirement, registering at around 1.4 Nm. The resulting angular displacement was of 25.1° ± 0.3°. The observed behaviour resembled that of the linear displacement of the TCP; as the load increased, displacement decreased, and elongation increased (indicated by a shift to a higher negative angle in the starting position). Conversely, when the load was too low (e.g. 0.5 Nm), the device experienced saturation. The relation between the input power and displacement can be seen as a linear relation. For example, the linear equation for the 1.0 Nm load will be equal to:

$$\alpha = 0.1916\,(\mathrm{mA}) - 20.397 \tag{6}$$

where α is the angular displacement in degrees, furthermore the R^2 if the linear equation is 0.9896 and a RMSE of 0.556.

The values for τ_h and τ_c ranged between 19 and 30 s (figure 7(c)). Additionally, the relationship between input power and temperature resembled that of the single fibre configuration, having its maximum temperature at 83.7 °C ± 0.2 °C when the 240 mA was applied (figure 7(d)).

2.7. SWRR model

After acquiring experimental data from the SWRR prototype, a computer model was developed by establishing a connection between ROM and input power. For this purpose, the 1.0 Nm load scenario was selected, as it closely approximated to the required torque of 1.5 Nm when the weight of the foot is taken into account and offered the most significant ROM (25°, sufficient for full dorsiflexion). The input signal comprised the applied power, while the output signal represented the resulting angular displacement. This dataset was then processed using the System Identification Toolbox in MATLAB. The Toolbox produced a power-angular displacement transfer function denoted as TFPD(s). The best model was as follows:

$$\mathrm{TFDP}\,(s) = \frac{0.01406\,s + 0.000249}{s^4 + 0.6203\,s^3 + 0.0327\,s^2 + 0.0003954}. \tag{7}$$

The model provides an accuracy of 92.83%.

3. Control strategy and results

Utilising the transfer function $\mathrm{TFDP}\,(s)$, a PID controller was tuned with the aid of the Control System Toolbox in MATLAB. Subsequently, a closed-loop system with the PID controller was simulated in MATLAB/Simulink. The simulation was focused on minimising potential issues such as overshoot, controller settling error, and power requirements, as any such errors could lead to the incorrect application of force to the user, potentially causing harm. To attain the desired maximum ROM of 10°, it took 5 s, corresponding to an inverse

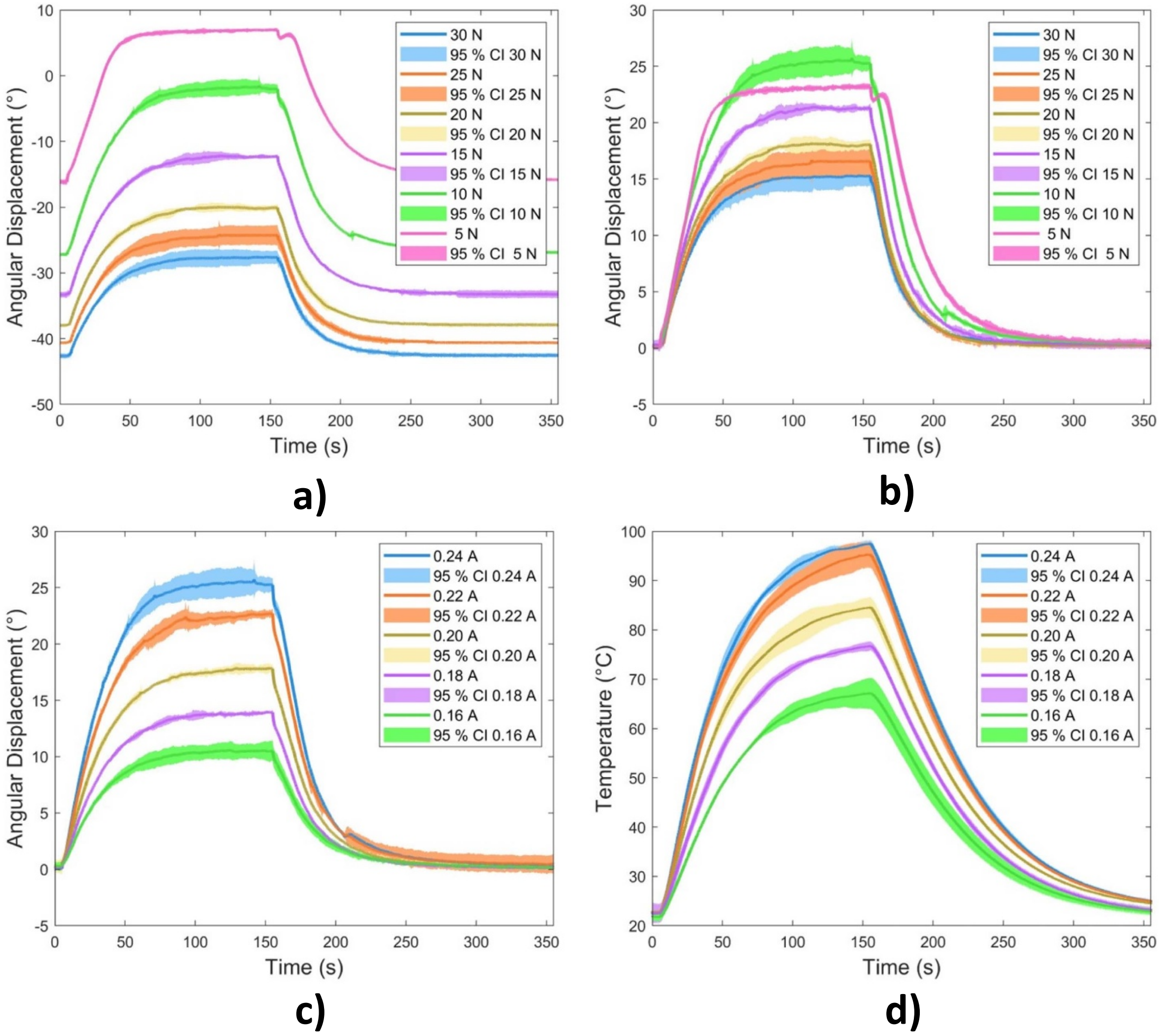

Figure 7. TCPs relations dummy test characteristics. (a) Angular displacement–torque relation when the maximum current of 240 mA is applied. (b) Angular displacement-power relation and (c) temperature-power relation when a torque of 1 Nm is applied. Confident intervals (CI) included.

of 0.2 Hz. The proportional, integral, and derivative components of the controller were configured as follows: $K\mathrm{p} = 17.14$, $K\mathrm{i} = 1.489$, $K\mathrm{d} = 33.84$.

After the closed-loop controller was tuned, it was implemented on an Arduino NANO microcontroller. A maximum power limit of 148 W was imposed, as determined by the capacity of the available power supply (60 V, 2.46 A). A pulse-width modulation strategy was employed to apply the requisite power. Three distinct tests were conducted: a step input test to evaluate the controller's performance, followed by a chirp test to assess the actuator's bandwidth. Lastly, an HRI was established using an electromyography (EMG) sensor MyoWare 1.0 (MyoWare) to capture muscle signals from the calf, demonstrating its potential as a control mechanism for the SWRR. Ag/AgCl electrodes were used, with bipolar electrodes situated on the belly of the tibialis anterior muscle and a reference electrode placed on the tibia. The EMG signal acquisition was performed with a 33 year-old male subject, using the same test bench employed for SWRR characterisation, now including the EMG sensor for the HRI test (as show in video S1).

3.1. Step signal

The reference signal for the step response was set at 10°, representing the ROM commonly observed during walking activities. In figure 8(a), the plot illustrates the position reference and the system's output when subjected to a step signal in the SWRR. The output closely tracks the reference signal; however, the system exhibits an overshoot response. It takes approximately 5 s to move from 0° to 10°. The power graph reveals that the controller initially requires the maximum available power of 148 W, which decreases to an average of 17 W (figure 8(b)).

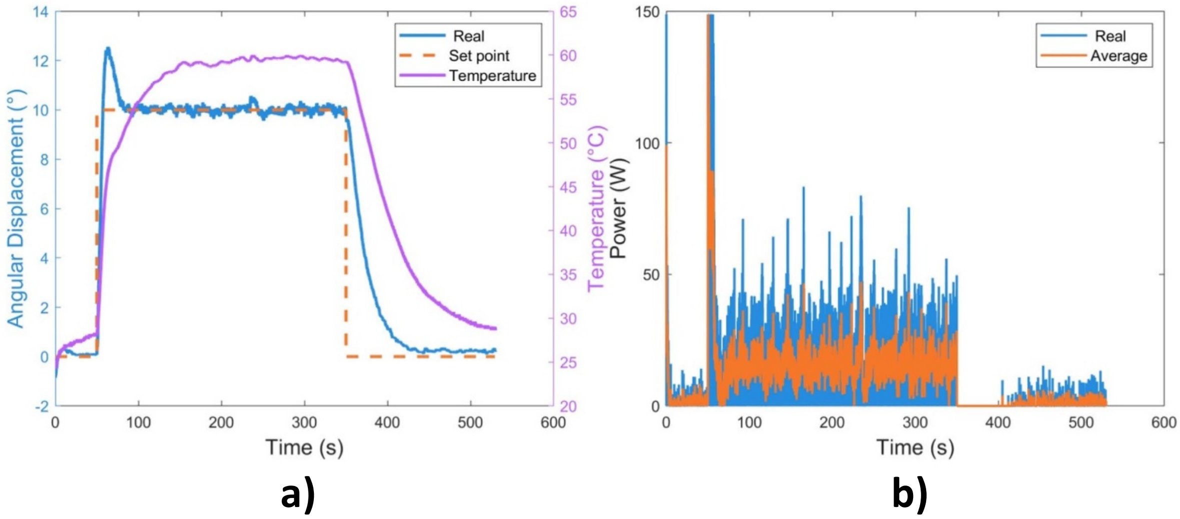

Figure 8. (a) Angular displacement and temperature of the SWRR after applying a step signal of 10° using a PID controller. (b) Power was applied to generate the 10° displacement.

Concerning temperature, it experiences a rapid rise initially but stabilises at 60 °C (figure 8(a)). Notably, the power and temperature values in the steady state closely resemble those observed during the open-loop test (with a step input of 180 mA).

3.2. Chirp signal

A chirp test was used to benchmark the working frequency of the whole system to understand its capabilities. A chirp signal consists of a sinusoidal sweep signal that varies its frequency over time, which can be expressed as follows:

$$\mathrm{chirp}\,(t) = A\sin\left[2\pi\left(\frac{c}{2}t^2 + f_0 t\right)\right]. \tag{8}$$

Here f_0 is the final frequency, A is the amplitude of the sinewave, t is the time, and c is the chirp rate, described by:

$$c = \frac{f_e - f_0}{T_s} \tag{9}$$

where f_e is the final frequency, and T_{s} is the time it takes to sweep from f_0 to f_e.

The sinewave had an amplitude of 10°, aligning with the required displacement, covering from a baseline of 0° to 10°. The frequency range was from 0.001 Hz to 0.1 Hz (figure 9(a)). The cutoff frequency was identified when the magnitude decreased to −3 dB. During the test, the actuator reached the −3 dB threshold at a frequency of 0.025 Hz (figure 9(b)). Regarding temperature, the actuator maintained an average temperature of 53 °C, indicating that the TCP struggled to track the chirp signal precisely (figure 9(c)). The power response was distinct, as the system attempted to operate at that frequency by oscillating between maximum power and zero (figure 9(d)). To enhance response time without requiring an external cooling system, an offset of 10° was introduced on the ROM, operating within the 10°–20° range. With this adjustment, the working frequency improved to 0.034 Hz, which was 1.36 times faster. Nevertheless, it still fell short of the target of 0.2 Hz.

3.3. EMG HRI

The EMG signal was sampled at a frequency of 20 Hz, corresponding to the speed of the serial communication. Using the MyoWare 1.0 sensor, two types of signals were obtained: the EMG raw signal and the EMG envelope (EMGe) signal. The latter serves as an amplitude-modulated representation of the raw signal. To identify muscle activation, a threshold of 150 mV was set for the EMGe signal, preventing errors coming from movement artefacts. The activation pattern remained active for 8 s to achieve the 10° movement, followed by 90 s to allow the system to cool down and return to the starting position, following a similar approach to Pittaccio *et al* [36].

From the graphical representations, it is evident that the system is triggered when the EMG envelope surpasses the 150 mV threshold (figures 10(a) and (c)). This activation prompts the utilisation of the entire power output, which relaxes over 90 s (figure 10(b)). These observations confirm that the SWRR device responds effectively to the EMG signal.

4. Discussion and conclusion

This study explored the proof of concept for a SWRR system using TCP AMSM. The research included an actuator characterisation and the design process to meet biomechanical requirements. The resulting device is lightweight, flexible, and compact, meeting the minimum biomechanical needs of children with physical disabilities. This includes achieving a 10° ROM within 5 s, a torque of 1.5 Nm and an HRI. However, several improvements are needed before this technology can be applied in rehabilitation settings.

The study's results indicate that the behaviour of single fibres is similar to the multifibre approach integrated in the

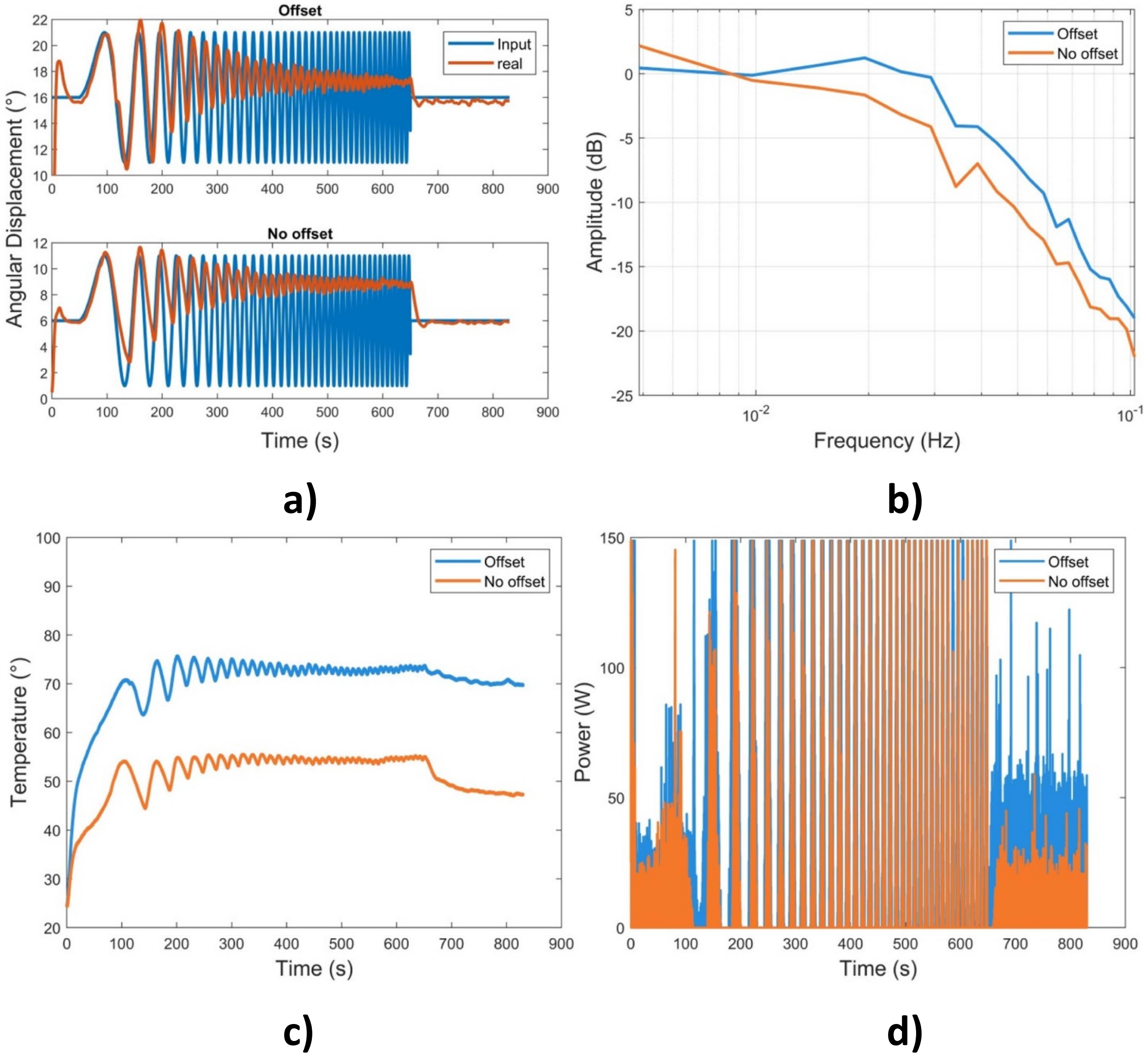

Figure 9. Chirp test results. (a) angular displacement of the SWRR following the chirp signal. (b) Magnitude decay in dB through frequency. (c) TCP temperature. (d) Power used by the SWRR.

SWRR. With differences in displacement and force as they translate into angular displacement and Torque. These differences are due to the mechanical design, and there's a trade-off between torque and displacement, as they are inversely proportional.

Despite the challenges, the technology appears highly adaptable, and many approaches can be taken to improve the performance. To enhance torque, incorporating additional fibres, as seen in previous TCP studies, is a viable direction [40, 41]. In this study, that approach was followed to get the required torque, as a single fibre would be insufficient to generate the necessary force.

Using longer actuators can significantly improve ROM, as this study shows. While the initial design requirement was a 10° ROM, the longer actuators enabled an impressive 25.18° ROM, effectively covering the full dorsiflexion range. This approach offers an additional advantage, as previously emphasised by Gonzalez *et al* [42], which is the reduction in temperature. This temperature control is vital for ensuring the device's safety during use. It is worth noting that the pain threshold for human skin at the dermal/epidermal layer is approximately 44 °C [27]. In this context, when considering the 10° ROM, the temperature was 65 °C lower compared to the temperatures reached when the actuator operated at its maximum stroke, which often exceeded 90 °C. Nonetheless, if the device is intended for use with children, the incorporation of an insulation layer, such as Polytetrafluoroethylene, is advisable to ensure optimal comfort and safety [43].

Nevertheless, coming from equations (2) and (5), the variation of r affect the linear displacement need to generate an angular displacement and the toque in an inverse manner. Is possible to improve this factor by tunning these distances, in the case of the study the r was chosen to be as small as possible because is the technology is envisioned to be used as a fabric that will be incorporated in clothes like socks.

The primary challenge associated with this technology pertains to its reaction time. However, this initial disadvantage could be solved by dividing this problem into two

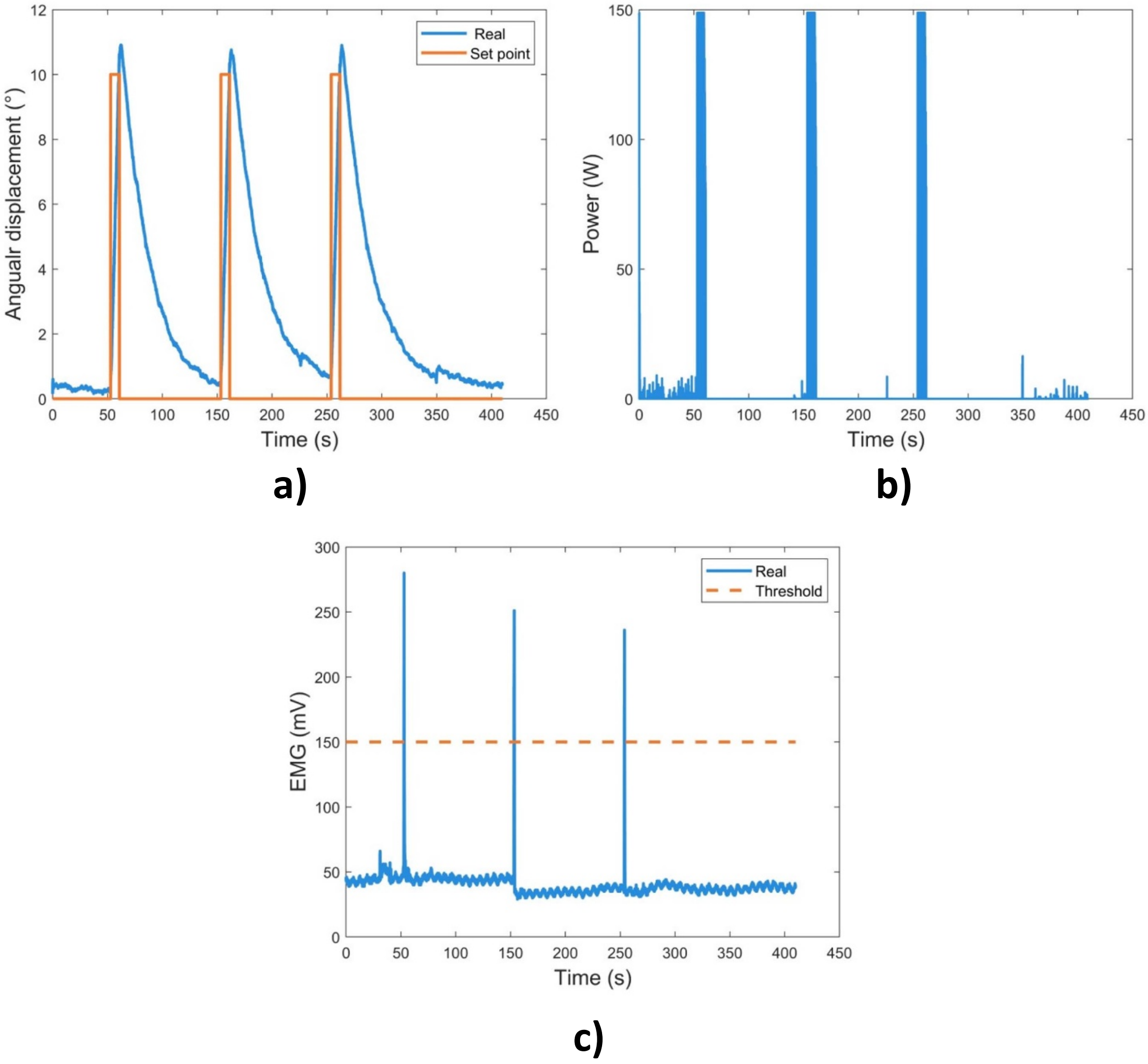

Figure 10. (a) Angular displacement generated after the EMG threshold was surpassed. (b) Power consumption of the SWRR during the EMG activation. (c) An EMG signal is used to trigger the SWRR.

distinct aspects due to the actuator's unidirectional nature, where applying power triggers contraction but cannot control elongation.

On one side, accelerating the contraction time necessitates increased applied power, leading to higher temperatures more quickly. The critical constraint lies in the need to carefully regulate this applied power to prevent heat-induced damage to the actuator. The research demonstrated that implementing the suggested control strategy allowed faster speeds without harming the actuator, preventing the fibre from overheating and burning [29]. Nevertheless, this approach demands substantial power levels to achieve rapid responses, often exceeding 100 Watts. This power requirement poses a challenge given the limitations of current battery technology. Nonetheless, advancements in energy storage and transmission are ongoing, promising improvements in energy density and battery miniaturisation [44–46].

On the other hand, addressing the relaxation phase poses a more complex challenge. This research sought to optimise the device's cooling process without external systems, relying on convective airflow. These optimisations involved creating sufficient spacing between each actuator to prevent heat transfer between individual fibres [40]. Regrettably, this consideration is counterproductive in the design as it limits the number of fibres used in the SWRR to produce higher torques.

Additionally, it was experimented with operating within an optimal temperature range, introducing an offset from the initial working point (from 0° to 10°) to achieve a faster movement previously investigated by Gonzalez *et al* [42]. This approach increased the frequency by 1.36 times. However, it did not significantly improve due to the actuator's considerably slower natural frequency than the required frequencies (0.02 Hz in TCP versus 1 Hz in walking activity).

Two potential alternatives come to light to address this issue. The first is incorporating a cooling system, as seen in numerous TCP research studies [47, 48]. The second option involves adopting agonist–antagonist muscle systems [43, 49]. However, it is important to note that these approaches entail increased system complexity, requiring additional components that expand the system's size and weight. Furthermore, it necessitates more sophisticated control strategies to activate each component as needed.

Finally, another crucial facet of SWRR technology is the HCI. To demonstrate the device's feasibility, a straightforward EMG HCI was implemented, showcasing the technology's capabilities. This approach allowed system activation to be controlled based on the user's intent through muscle activation, a pivotal component of rehabilitation therapy that enhances user engagement. Looking ahead, it would be compelling to explore the incorporation of various wearable sensor technologies in conjunction with TCP technology to create SWRR devices that can seamlessly integrate into the daily lives of children. This advancement holds the promise of substantially improving their overall quality of life.

This study presents innovative components to design paediatric ankle SWRRs. These elements provide solutions to specific issues of traditional exoskeletons (weight and compliance) and can be translated to develop SWRR for different purposes. Nevertheless, as discussed, the technology still needs to be improved for its widespread adoption in rehabilitation settings. Additionally, it is essential to collaborate closely with human users to understand better and address any technology shortcomings.

Data availability statement

All data that support the findings of this study are included within the article (and any supplementary files).

Acknowledgments

This work was partially supported by 'Consejo Nacional de Ciencia y Tecnologia' of Mexico (No. 739850). A G V thanks Nick Van Der Geest for her help in the CAD design of the Braces.

Conflict of interest

The authors declare no conflict of interest.

Limitations

The current device was not tested on paediatric patients due to ethical limitations. Hence, the performance shown in the study could change when applied to paediatric patients.

In the case of the used metric from the biomechanical requirements, all the analysed metrics were the minimum requirements for all the attributes. However, it recognised the need for additional refinement before clinical use. This research is proof of concept of the technology aimed to explore its strengths and limitations, emphasising the ongoing work required for its potential widespread clinical implementation.

Ethics declaration

The authors declare that the research was compliant with the New Zealand code of ethics.

ORCID iDs

Alberto Gonzalez-Vazquez https://orcid.org/0000-0001-6514-7888
Lorenzo Garcia https://orcid.org/0000-0002-1122-497X

References

[1] Chen D, Huang M, Yin Y, Gui D, Gu Y, Zhuang T, Chen C and Huo K 2022 Risk factors of cerebral palsy in children: a systematic review and meta-analysis *Trans. Pediatr.* **11** 556

[2] Abgottspon S, Thaqi Q, Steiner L, Slavova N, Grunt S, Steinlin M and Everts R 2022 Effect of age at pediatric stroke on long-term cognitive outcome *Neurology* **98** e721–9

[3] Ryan J L, Zhou C, Levac D E, Fehlings D L, Beal D S, Hung R and Wright F V 2023 Gross motor change after inpatient rehabilitation for children with acquired brain injury: a 10-year retrospective review *Dev. Med. Child Neurol.* **65** 953–60

[4] Vandekerckhove I *et al* 2022 Longitudinal alterations in gait features in growing children with Duchenne muscular dystrophy *Front. Hum. Neurosci.* **16** 861136

[5] Scheijmans F E *et al* 2022 Population-based assessment of nusinersen efficacy in children with spinal muscular atrophy: a 3-year follow-up study *Brain Commun.* **4** fcac269

[6] Hall M L and Lobo M A 2018 Design and development of the first exoskeletal garment to enhance arm mobility for children with movement impairments *Assist. Technol.* **30** 251–8

[7] Gmelig Meyling C, Verschuren O, Rentinck I R, Engelbert R H and Gorter J W 2022 Physical rehabilitation interventions in children with acquired brain injury: a scoping review *Dev. Med. Child Neurol.* **64** 40–48

[8] Hawe R L, Kuczynski A M, Kirton A and Dukelow S P 2020 Assessment of bilateral motor skills and visuospatial attention in children with perinatal stroke using a robotic object hitting task *J. Neuroeng. Rehabil.* **17** 1–12

[9] Eguren D, Cestari M, Luu T P, Kilicarslan A, Steele A and Contreras-Vidal J L 2019 Design of a customizable, modular pediatric exoskeleton for rehabilitation and mobility *2019 IEEE Int. Conf. on Systems, Man and Cybernetics (SMC)* (IEEE) pp 2411–6

[10] Gonzalez-Vazquez A, Garcia L, Kilby J and McNair P 2023 Soft wearable rehabilitation robots with artificial muscles based on smart materials: a review *Adv. Intell. Syst.* **5** 2200159

[11] Gonzalez A, Garcia L, Kilby J and McNair P 2021 Robotic devices for paediatric rehabilitation: a review of design features *Biomed. Eng. Online* **20** 1–33

[12] Patane F, Rossi S, Del Sette F, Taborri J and Cappa P 2017 WAKE-Up exoskeleton to assist children with cerebral palsy: design and preliminary evaluation in level walking *IEEE Trans. Neural Syst. Rehabil. Eng.* **25** 906–16

[13] Rossi S, Colazza A, Petrarca M, Castelli E, Cappa P and Krebs H I 2013 Feasibility study of a wearable exoskeleton for children: is the gait altered by adding masses on lower limbs? *PLoS One* **8** e73139

[14] Lerner Z F, Gasparri G M, Bair M O, Lawson J L, Luque J, Harvey T A and Lerner A T 2018 An untethered ankle exoskeleton improves walking economy in a pilot study of

individuals with cerebral palsy *IEEE Trans. Neural Syst. Rehabil. Eng.* **26** 1985–93

[15] Rus D and Tolley M T 2015 Design, fabrication and control of soft robots *Nature* **521** 467–75

[16] Bahl S, Nagar H, Singh I and Sehgal S 2020 Smart materials types, properties and applications: a review *Mater. Today Proc.* **28** 1302–6

[17] Bengisu M and Ferrara M 2018 *Materials that Move: Smart Materials, Intelligent Design* (Springer)

[18] Nematollahi M, Baghbaderani K S, Amerinatanzi A, Zamanian H and Elahinia M 2019 Application of NiTi in assistive and rehabilitation devices: a review *Bioengineering* **6** 37

[19] Dong T-Y, Zhang X-L and Liu T 2018 Artificial muscles for wearable assistance and rehabilitation *Front. Inf. Technol. Electron. Eng.* **19** 1303–15

[20] Mirvakili S M and Hunter I W 2018 Artificial muscles: mechanisms, applications, and challenges *Adv. Mater.* **30** 1704407

[21] Shi B, Chen X, Yue Z, Yin S, Weng Q, Zhang X, Wang J and Wen W 2019 Wearable ankle robots in post-stroke rehabilitation of gait: a systematic review *Front. Neurorobot.* **13** 63

[22] Zhang J, Sheng J, O'Neill C T, Walsh C J, Wood R J, Ryu J-H, Desai J P and Yip M C 2019 Robotic artificial muscles: current progress and future perspectives *IEEE Trans. Robot.* **35** 761–81

[23] Veale A J and Xie S Q 2016 Towards compliant and wearable robotic orthoses: a review of current and emerging actuator technologies *Med. Eng. Phys.* **38** 317–25

[24] Behboodi A and Lee S 2019 Benchmarking of a commercially available stacked dielectric elastomer as an alternative actuator for rehabilitation robotic exoskeletons *2019 IEEE 16th Int. Conf. on Rehabilitation Robotics (ICORR)* (IEEE) pp 499–505

[25] Jani J M, Leary M, Subic A and Gibson M A 2014 A review of shape memory alloy research, applications and opportunities *Mater. Des.* **56** 1078–113

[26] Haines C S *et al* 2014 Artificial muscles from fishing line and sewing thread *Science* **343** 868–72

[27] Saharan L, de Andrade M J, Saleem W, Baughman R H and Tadesse Y 2017 iGrab: hand orthosis powered by twisted and coiled polymer muscles *Smart Mater. Struct.* **26** 105048

[28] Sutton L, Moein H, Rafiee A, Madden J D and Menon C 2016 Design of an assistive wrist orthosis using conductive nylon actuators *2016 6th IEEE Int. Conf. on Biomedical Robotics and Biomechatronics (Biorob)* (IEEE) pp 1074–9

[29] Patiño A G, Ferrone A, Gastélum C G D and Menon C 2018 A novel biomedical technology based on the use of artificial muscles to assist with hand functions *2018 IEEE 9th Annual Information Technology, Electronics and Mobile Communication Conf. (IEMCON)* (IEEE) pp 620–5

[30] Sarajchi M, Al-Hares M and Sirlantzis K 2021 Wearable lower-limb exoskeleton for children with cerebral palsy: a systematic review of mechanical design, actuation type, control strategy, and clinical evaluation *IEEE Trans. Neural Syst. Rehabil. Eng.* **29** 2695–720

[31] Chossat J B, Chen D K Y, Park Y L and Shull P B 2019 Soft wearable skin-stretch device for haptic feedback using twisted and coiled polymer actuators *IEEE Trans. Haptics* **24** 521–32

[32] Brockett C L and Chapman G J 2016 Biomechanics of the ankle *Orthop. Trauma* **30** 232–8

[33] Alvarez-Perez M G, Garcia-Murillo M A and Cervantes-Sanchez J J 2019 Robot-assisted ankle rehabilitation: a review *Disability Rehabil. Assist. Technol.* **15** 1–15

[34] Peng Q, Park H-S, Shah P, Wilson N, Ren Y, Wu Y-N, Liu J, Gaebler-Spira D J and Zhang L-Q 2011 Quantitative evaluations of ankle spasticity and stiffness in neurological disorders using manual spasticity evaluator *J. Rehabil. Res. Dev.* **48** 473

[35] Chung S G, Van Rey E, Bai Z, Roth E J and Zhang L-Q 2004 Biomechanic changes in passive properties of hemiplegic ankles with spastic hypertonia *Arch. Phys. Med. Rehabil.* **85** 1638–46

[36] Pittaccio S, Viscuso S, Rossini M, Magoni L, Pirovano S, Villa E, Besseghini S and Molteni F 2009 SHADE: a shape-memory-activated device promoting ankle dorsiflexion *J. Mater. Eng. Perform.* **18** 824–30

[37] Chen S-H *et al* 2016 Assistive control system for upper limb rehabilitation robot *IEEE Trans. Neural Syst. Rehabil. Eng.* **24** 1199–209

[38] Organization W H 2020 Growth reference 5–19 years (available at: www.who.int/growthref/en/)

[39] Winter D A 2009 *Biomechanics and Motor Control of Human Movement* (Wiley)

[40] Haines C S and Niemeyer G Closed-loop temperature control of nylon artificial muscles 2018 *2018 IEEE/RSJ Int. Conf. on Intelligent Robots and Systems (IROS)* (IEEE) pp 6980–5

[41] Murphy V, Edmonds B P and Trejos A L 2021 Characterisation and control of a woven biomimetic actuator for wearable neurorehabilitative devices *Actuators* **10** 37

[42] Gonzalez A, Garcia L and Kilby J 2023 Improved performance in temperature and speed of TCP artificial muscles for soft wearables robots by length modification *Smart Mater. Struct.* **32** 085002

[43] Copaci D, Martín F, Moreno L and Blanco D 2019 SMA based elbow exoskeleton for rehabilitation therapy and patient evaluation *IEEE Access* **7** 31473–84

[44] Subasinghage K, Gunawardane N, Kularatna N and Moradian M 2022 Modern supercapacitors technologies and their applicability in mature electrical engineering applications *Energies* **15** 7752

[45] Ma L *et al* 2019 Achieving both high voltage and high capacity in aqueous zinc-ion battery for record high energy density *Adv. Funct. Mater.* **29** 1906142

[46] Liu Q, Zhang G, Chen N, Feng X, Wang C, Wang J, Jin X and Qu L 2020 The first flexible dual-ion microbattery demonstrates superior capacity and ultrahigh energy density: small and powerful *Adv. Funct. Mater.* **30** 2002086

[47] Edmonds B P and Trejos A L 2019 Design of an active cooling system for thermally activated soft actuators *2019 IEEE 16th Int. Conf. on Rehabilitation Robotics (ICORR)* (IEEE) pp 368–73

[48] Yip M C and Niemeyer G 2017 On the control and properties of supercoiled polymer artificial muscles *IEEE Trans. Robot.* **33** 689–99

[49] Park S J, Choi K, Rodrigue H and Park C H 2022 Fabric muscle with a cooling acceleration structure for upper limb assistance soft exosuits *Sci. Rep.* **12** 1–13